Physical and chemical properties of black carbon and organic matter from different sources using aerodynamic aerosol classification

Dawei Hu[1,*], M. Rami Alfarra[1,2,#], Kate Szpek[3], Justin M. Langridge[3], Michael I. Cotterell[5], Claire Belcher[4], Ian Rule[4], Zixia Liu[4], Chenjie Yu[1], Yunqi Shao[1], Aristeidis Voliotis[1], Mao Du[1], Brett Smith[6], Greg Smallwood[6], Prem Lobo[6], Dantong Liu[7], Jim M. Haywood[4], Hugh Coe[1], James D. Allan[1,2,*]

[1]Department of Earth and Environmental Sciences, University of Manchester, UK.

[2]National Centre for Atmospheric Science, University of Manchester, Manchester, UK.

[3]Observation Based Research, Met Office, Exeter, UK

10   [4]College for Engineering, Mathematics and Physical Sciences, University of Exeter, Exeter, UK

[5]School of Chemistry, University of Bristol, Bristol, UK

[6]Metrology Research Centre, National Research Council Canada, Ottawa, Canada.

[7]Department of Atmospheric Sciences, School of Earth Sciences, Zhejiang University, Hangzhou, Zhejiang, China.

15   [#]Currently at Qatar Environment and Energy Research Institute (QEERI), Hamad Bin Khalifa University (HBKU), Doha, Qatar.

[*]Correspondence to: dawei.hu@manchester.ac.uk; james.allan@manchester.ac.uk

20   **Abstract.**

The physical and chemical properties of black carbon (BC) and organic aerosols are important for predicting their radiative forcing in the atmosphere. During the Soot Aerodynamic Size Selection for Optical properties (SASSO) project and a EUROCHAMP-2020 transnational access project, different types of light absorbing carbon were studied,

25   including BC from catalytically stripped diesel exhaust, a flame burner, a colloidal graphite standard (Aquadag), and from controlled flaming wood combustion. Brown carbon (BrC) was also investigated in the form of organic aerosol emissions from wood burning (pyrolysis and smouldering) and from the nitration of secondary organic aerosol (SOA) proxies

produced in a photochemical reaction chamber. Here we present insights into the physical

30 and chemical properties of the aerosols, with optical properties being presented in subsequent

publications. The dynamic shape factor (χ) of BC particles and material density (ρ_m) of

organic aerosols were investigated by coupling a charging-free Aerodynamic Aerosol

Classifier (AAC) with a Centrifugal Particle Mass Analyzer (CPMA) and Scanning Mobility

Particle Sizer (SMPS). The morphology of BC particles was captured by transmission

35 electron microscopy (TEM). For BC particles from the diesel engine and flame burner

emissions, the primary spherule sizes were similar, around 20 nm. With increasing particle

size, BC particles adopted more collapsed/compacted morphologies for the former source but

tended to show more aggregated morphologies for the latter source. For particles emitted

from the combustion of dry wood samples, the χ of BC particles and the ρ_m of organic

40 aerosols were observed in the ranges 1.8-2.17 and 1.22-1.32 g/cm^3, respectively. Similarly,

for wet wood samples, the χ and ρ_m ranges were 1.2-1.85 and 1.44-1.60 g/cm^3, respectively.

Aerosol mass spectrometry measurements show no clear difference in mass spectra of the

organic aerosols in individual burn phases (pyrolysis or smouldering phase) with the moisture

content of the wood samples. This implies that the effect moisture has on the organic

45 chemical profile of wood burning emissions is through changing the durations of the different

phases of the burn cycle, not through the chemical modification of the individual phases. In

this study, the incandescence signal of a Single Particle Soot Photometer (SP2) was calibrated

with three different types of BC particles and compared with that from an Aquadag standard

that is commonly used to calibrate SP2 incandescence to a BC mass. A correction factor is

50 defined as the ratio of the incandescence signal from an alternative BC source to that from the

Aquadag standard, and took values of 0.82 (or 0.79), 0.88 and 0.84-0.91 for the BC particles

emitted from the diesel engine running under hot (or cold idle) conditions, the flame burner

and wood combustion, respectively. These correction factors account for differences in instrument response to BC from different sources compared to the standardised Aquadag

55 calibration and are more appropriate than the common value of 0.75 recommended by Laborde et al. (2012b) when deriving the mass concentration of BC emitted from diesel engines. Quantifying the correction factor for many types of BC particles found commonly in the atmosphere may enable better constraints to be placed on this factor depending on the BC source being sampled, and thus improve the accuracy of future SP2 measurements of BC

60 mass concentrations.

1 Introduction

Black carbon (BC) and brown carbon (BrC) aerosols are widely investigated components of atmospheric aerosol because they can absorb solar radiation and heat the atmosphere causing a positive radiative forcing of climate (Bond and Bergstrom, 2006;Liu et al., 2020a;Bond et

65 al., 2013;Haywood and Shine, 1995). BC is emitted by incomplete combustion processes, including from anthropogenic (e.g., diesel engines) and natural (e.g., flaming combustion in wildfires) sources. BrC aerosols are organic aerosols that absorb light in the visible and near-UV regions, and are emitted directly from biomass burning, biofuel combustion and biogenic processes (Ramanathan et al., 2007;Bond, 2001;Andreae and Crutzen, 1997), or formed

70 through the chemical reaction processes in the atmosphere, including the nitration of aromatic compounds (Zhang et al., 2013;Lu et al., 2011;Harrison et al., 2005;Lin et al., 2015), formation of higher molecular weight oligomers by acid catalysed aldol-condensation reactions (Shapiro et al., 2009;Bones et al., 2010;Noziere and Esteve, 2007), and reactions of ammonium-containing species with (di-)carbonyl species (Maxut et al., 2015;Powelson et al.,

75 2014;De Haan et al., 2017). Typically, the light absorption coefficient for BC is wavelength independent over the visible spectrum, but is strongly wavelength dependent for BrC that is

characterised by increasing absorption with progressively shorter visible wavelengths (Kirchstetter et al., 2004;Corbin et al., 2019;Voliotis et al., 2017).

Although BC and BrC are very important for climate, they are poorly represented in atmospheric models (Zuidema et al., 2016). This is in part due to the complex microphysical properties of BC and the lack of accurate refractive index (RI) descriptions for both BC and BrC (Liu et al., 2020b). In recent decades, the RI of BC or BrC was derived by measuring the optical properties for particles of controlled size, with studies commonly utilising the differential mobility analyser (DMA) to classify charged aerosols on their electrical mobility diameter. However, the DMA approach suffers from transmitting a highly polydisperse and multi-modal size distribution; this technique relies on the selection of particles on their electrical mobility from an aerosol ensemble with a bipolar charge distribution, transmitting particles with a single electrical mobility that can be achieved for multiple combinations of particle charge and size. Thus, in addition to singly-charged particles of the desired size, larger particles with doublet or triplet charge states are selected which can impact optical measurements significantly. Careful consideration of the impacts of multiply charged particles in subsequent RI derivations can go some way to correcting for these impacts, but this nevertheless remains a significant contributor to uncertainty in the resulting RI (Cotterell et al., 2020;Zarzana et al., 2014;Miles et al., 2011). To solve this problem, during the Soot Aerodynamic Size Selection for Optical properties (SASSO) project, a pioneering approach utilising the Aerodynamic Aerosol Classifier (AAC) was used to provide 'true' monodisperse size selection of aerosols for optical evaluation (Tavakoli et al., 2014), enabling authoritative retrievals of RI for isolated BC and BrC from wood burning, diesel combustion and secondary organic aerosol (SOA) formation. Specifically, SASSO has pioneered the AAC size selection of these aerosol emissions prior to optical interrogation using cavity ring-down

and photoacoustic spectroscopy with the EXtinction, SCattering and Absorption of Light for AirBorne Aerosol Research (EXSCALABAR) instrumentation, custom-built by the Met Office (Cotterell et al., 2020;Cotterell et al., 2019a;Davies et al., 2018). Moreover, as the presence of non- or weakly-absorbing coatings can increase the per-mass absorption of the

105 BC particles, the so-called "lensing effect" was also tested by condensation of two types of organic materials onto bare BC, one is non-absorbing SOA and one is BrC (Taylor et al., 2020;Liu et al., 2017).

An important consideration in the retrieval of refractive indices from optical spectroscopy data is the aerosol morphology and mixing state. Accurate descriptions of these properties are

110 needed before the RI of BC and organic aerosols are derived. Indeed, these properties of morphology and mixing state are often probed for combustion-derived aerosols using the Single Particle Soot Photometer (SP2) instrument. SASSO has put a SP2 downstream of the AAC to measure the refractory BC (rBC) mass and optical size of individual BC, but the SP2 needs an empirical calibration to retrieve the rBC mass from the incandescence signal

115 (Laborde et al., 2012a). As the sensitivity of the SP2 incandescence signal differs between different BC types, which makes the complexity of the calibration methods, the conventional way to calibrate the incandescence channel of SP2 is using the mono-dispersed Aquadag standards (Acheson Inc. USA), and then corrected for ambient rBC by a constant factor of 0.75 (Laborde et al., 2012b). However, very few experiments linking Aquadag calibrated SP2

120 BC mass to the BC mass from sources of relevance to atmospheric or combustion processes. Thus, the purpose of this paper is to determine the physical and chemical properties of BC and organic aerosols from different combustion sources representing the combustion of gas (methane), liquid (diesel) and solid (wood), and to examine the variation in SP2 constants for BC particles generated by these combustion sources to enable accurate characterizations of

125 BC mass concentrations and mixing state in future studies. The key objectives of this work

are: (1) Derive the dynamic shape factor of BC particles and material density for organic

aerosols; (2) Determine mass spectral profiles of organic aerosols produced from wood

combustion from an aerosol mass spectrometer (AMS); (3) Explore the restructuring of BC

particles in response to the controlled coating and humidification of aerosol samples; and (4)

130 Investigate the response of the SP2 incandescence signal to different types of the BC particles.

The characterisation and parameterisation of the optical properties of the particles will be the

subject of a future publication.

2 Experimental setup and methods

Figure 1 shows our novel instrument configuration during SASSO. We used the AAC to

135 classify aerosols on their aerodynamic size prior to to characterizing the particle size

distribution, chemical composition, aerosol mixing state and optical properties for the AAC-

selected aerosols, thus enabling optical properties – in particular refractive index – to be

determined with much lower uncertainty than has been achieved previously. The Centrifugal

Particle Mass Analyzer (CPMA) and Scanning Mobility Particle Sizer (SMPS) sampled

140 aerosols downstream of the AAC to measure the mass and mobility size distributions of the

AAC-selected particles. A Nafion humidifier and a custom designed thermal denuder (TD)

were used for the BC restructuring test.

2.1 Instrumentation

2.1.1 AAC

145 The AAC (Cambustion Ltd, Cambridge, UK) is the ideal instrument for selecting a truly

monodisperse aerosol from a polydisperse source. The AAC uses a centrifugal force and

sheath flow between two concentric rotating cylinders to produce a monodisperse aerosol

classified by aerodynamic diameter, and does not suffer from charge-related phenomena that are associated with the CPMA and DMA. This technique allows online size classification of

150 particles without requiring them to be electrically charged, and advantageously allows selection of particles (between 25 nm and >5000 nm) within a narrow range of aerodynamic diameters. The detailed information regarding the principle of AAC can be found in Tavakoli et al. (2014).

2.1.2 EXSCALABAR

155 The EXSCALABAR instrument used in this work was developed by the Met Office (Exeter, UK), which can be operated in both the laboratory and from the UK atmospheric research aircraft (FAAM BAe-146). The operating principle of EXSCALABAR has been described in detail in previous papers (Davies et al., 2018;Cotterell et al., 2020;Cotterell et al., 2019a;Cotterell et al., 2019b). In brief, the instrument uses cavity ring-down spectroscopy

160 (CRDS) to measure the dry aerosol extinction at 405 and 658 nm wavelengths and photoacoustic spectroscopy (PAS) to measure the dry aerosol absorption coefficient at the wavelengths of 405, 514 and 658 nm wavelengths. For deployment during SASSO, all cells shared common sample conditioning; the aerosol sample relative humidity was reduced to <10% by passing through a Nafion drier (Perma Pure LLC) and Ozone and NOx were

165 removed by an activated charcoal "honeycomb" scrubber (custom-built in-house). The sample passed through an impactor (Brechtel Manufacturing Inc., custom built for an 8 L min^{-1} volumetric flow rate) with aerodynamic cut-off (D50) of 1.3 μm before being drawn through a series of flow splitters that evenly distributed the aerosol-laden air samples to the various optical spectrometers, each operating at 1 L min^{-1}. For both the 405 nm and 658 nm

170 wavelengths, the PAS cells were mounted downstream of the CRDS cells (CRDS-PAS) i.e. the sample passed through the CRDS cell before entering the PAS cell of the same

wavelength. All other cells operated in a parallel flow configuration. During the wood

combustion experiments, a Condensation Particle Counter (CPC) (Model 3776, TSI, USA)

was put in series after the 405-nm CRDS-PAS to measure the number concentration of

175 particles contributing to the extinction and absorption signal. For an additional 405-nm

CRDS spectrometer, the aerosol sample passed through a HEPA filter prior to sampling to

provide a continuous measurement of the baseline and highlight the presence of any gaseous

absorbers affecting measurements at that wavelength. CRDS and PAS measurements rely on

characterization of the aerosol-free background. Before and after each wood combustion

180 experiment (run), sample flow was routed through a HEPA filter immediately after

EXSCALABAR's common sample inlet section to provide baseline measurements of empty-

cavity ring-down time and background photoacoustic response for all CRDS and PAS

spectrometers, respectively. During the Manchester chamber experiments, the CPC was fitted

in parallel with the sample lines, and automated baseline measurements were made every 10

185 minutes. PAS cells with improved sensitivity – as described by Cotterell et al. (2019b) – were

gradually implemented during 2019; only the 405 nm dry absorption measurement used the

new cells during the Wildfire lab wood combustion experiments, but all cells were upgraded

by the start of the Manchester aerosol chamber experiments. The PAS cells were calibrated

using Ozone before and after each set of experiments as well as at least every working week

190 during the experimental periods, as described by Davies et al. (2018) and discussed further by

Cotterell et al. (2019a).

2.1.3 SP2

The refractory black carbon (rBC) mass concentration was measured by a SP2 (Droplet

Measurement Technologies, Colorado, USA). The SP2 uses the laser-induced incandescence

195 to measure the rBC mass and optical size of individual BC particles. The SP2 consists of an

intense intra-cavity laser operating at a wavelength of 1064 nm and four optical detectors. Particles were drawn into the measurement chamber through a capillary, restricted with a particle free sheath flow and focused into a jet. The particle jet passed through the center of an intra-cavity laser beam operating at 1064 nm. The particle size can be determined by

200   detecting the scattered laser signal by particles, with the scattering intensity maximum related to the optical particle diameter through a calibration using polystyrene latex spheres. Because the scattering signal of the absorbing particle will be distorted during its transit through the laser beam due to the mass loss by laser heating, the leading edge scattering signal before the onset of volatilisation is extrapolated to reconstruct the scattering signal of the absorbing

205   particles particle (Gao et al., 2007;Liu et al., 2014). This calibration was performed at the start of the measurement campaign. For those particles which contain absorbing materials such as the refractive BC, they will absorb 1064 nm light and then heat up and emit visible thermal radiation (incandesce). This incandescence signal is directly proportional to the mass of rBC through a calibration (Liu et al., 2010) with generated BC aerosols of known or

210   independently-measured mass; we investigated the effectiveness of this calibration from different types of BC particles in this study and report the outcomes of these investigations in Sect. 3.1.

2.1.4 High-Resolution Aerosol Mass Spectrometer (HR-AMS)

Non-refractory aerosol chemical compositions including sulfate, nitrate, ammonium, chloride,

215   and organics were measured by a HR-AMS in real time. The HR-AMS was operated in fast-mode to capture the fast transition of the combustion phase during the wood combustion experiment. The instrument operation and data analysis of HR-AMS has been described in detail elsewhere (Alfarra et al., 2006; Allan et al., 2003, 2004; DeCarlo et al., 2006). The ionization efficiency of the AMS was calibrated using monodisperse ammonium nitrate

220   particles according to the method described by Jayne et al. (2000) at various times during the

experimental periods.

2.1.5 CPMA

The CPMA (Cambustion Ltd., Cambridge, UK) uses opposing electrical and centrifugal

fields to classify particles according to their mass-to-charge ratio. The ability to vary the

225   electrical field and rotation speed enables particle selection based on their mass. The

principles and operation of the CPMA have been described elsewhere (Olfert and Collings,

2005;Olfert et al., 2006). Combining the CPMA with a CPC (Model 3776, TSI, USA) and

scanning across the mass range of interest provides the bulk aerosol mass size distribution.

2.1.6 SMPS

230   The SMPS (TSI, 3080, USA) is based on the principle of the electrical mobility of a charged

particle in an electric field. A bipolar charge distribution was imparted to the aerosol particles

entering classifier using a Kr-85 neutralizer. The charged aerosols then enter a DMA where

they were classified according to their electrical mobility, with only particles of a narrow

range of mobility exiting through an output slit. This aerosol sample then passed to a CPC

235   which determined the particle concentration at the selected mobility diameter. The DMA-

selected mobility diameter was scanned and the transmitted particle number concentration

was recorded. These measurements were then passed through an inversion algorithm that

accounted for multiple charge effects that lead to multimodal size distributions for a selected

mobility diameter, enabling the particle mobility size distribution to be measured. In this

240   study, aerosol size distributions in the diameter range from 14.9 to 673.2 nm were measured

by a commercial SMPS (TSI 3080, USA) with sheath and sample flow rates of 3 L min^{-1} and

0.3 L min^{-1}, respectively.

2.1.7 Transmission electron microscopy (TEM) sampling and analysis

To investigate morphological properties, BC particles were collected on carbon coated copper

245   grids using an electrostatic sampler (ESPnano, DASH Inc., USA) (Miller et al., 2010) for

transmission electron microscopy (TEM) analysis. The grids were analyzed using a FEI Titan

operated at 300 kV. Several areas of the grid were imaged to provide representative images

for each sample since both the grid film and particles contained carbon.

2.1.8 Thermal denuder (TD)

250   We explored the impacts of the partitioning of coating materials on the structure of BC. For

this BC restructuring experiment, a thermal denuder was utilised to remove the coating

materials on coated BC particles. The home-built TD consisted of a stainless steel tube in a

temperature controlled furnace (Voliotis et al., 2021). The TD had a length of 0.97 m and an

internal diameter (ID) of 0.15 m. Aerosols entered and exited the TD unit via a cylindrical

255   0.12 m long and 0.037 m ID stainless steel compartment. The temperature in the heating

section (0.51 m × 0.15 m ID) was controlled by four PID controllers (Watlow EZ-ZONE)

with additional temperature sensors on the outside of the tube. The residence time of the air

sample in the heating section was ~31 s (corresponding to a 1.0 L min^{-1} flow rate). All

heating zones were set to 180 °C.

2.1.9 Nafion humidifier

260

The multi-tube Nafion humidifier in the Manchester home-made Hygroscopicity Tandem

Differential Mobility Analyser (HTDMA) system was used for the BC restructuring

experiment. The principle and configuration of the HTDMA system including the Nafion

humidifier flow system can be found in Good et al. (2010). The RH in the Nafion humidifier

265   was controlled by adjusting the relative mixing ratio of dry air from a compressed air source

with humidified air generated by bubbling compressed air through a water-filled glass bulb.

2.1.10 The Manchester Aerosol Chamber (MAC)

The Manchester Aerosol Chamber comprises an 18 m^3 collapsible Fluorinated ethylene

propylene Teflon bag (3m (H) × 3m (L) × 2m (W)). It was used by Alfarra et al. (2012) to

270   investigate the effect of photochemical aging and initial precursor concentration on the

composition and hygroscopic properties of secondary organic aerosol. The chamber was run

as a batch reactor in which the composition of the gaseous precursors, oxidising environment,

primary emissions or seed particles, relative humidity and temperature were controlled. Air

was supplied to the chamber by a blower at a flow of 3 m^3 min^{-1}. The air was dried and

275   filtered for gaseous impurities and particles using a series of Purafil (Purafil Inc., USA),

charcoal and HEPA filters (Donaldson Filtration, USA), prior to humidification with

ultrapure deionised water. Halogen bulbs and two 6 kW Xenon arc lamps were mounted on

the inside of the enclosure housing the bag, which was coated with a reflective space blanket

to maximise the irradiance in the bag and to ensure even illumination. The Xenon arc lamps

280   were mounted on two opposite sides of the enclosure at different heights. The combination of

illumination was tuned and evaluated to mimic the atmospheric actinic spectrum over the

wavelength range 290 - 800 nm, and had a maximum total actinic flux of 1.4×10^{14} (photon

s^{-1} m^{-2} nm^{-1}) over the region 460 - 600 nm. The calculated $j(O^1D)$ value during the reported

experiments was 1.23×10^{-5} s^{-1} (290 - 340 nm) and $j(NO_2)$ was 1.5×10^{-3} s^{-1} (290 - 422 nm).

285   The relatively large volume of the chamber allows the dilute sample can be held for several

hours without significant aerosol removal from wall losses, allowing the study of particles

introduced directly or formed within the chamber over a period of several hours. Further

details on the chamber are given by Alfarra et al. (2012).

2.1.11 Diesel Engine

290   The engine used in this study was a Volkswagen 1.9L SDI light duty diesel engine (EURO 4 car equivalent), mounted on a test rig (CM12; Armfield Ltd., Hampshire, UK) and coupled to an eddy current dynamometer. This setup was used for investigating the light absorption properties of black carbon aerosol by Liu et al. (2017) previously. The engine throttle and the load on the dynamometer were controlled with dedicated software. The engine exhaust was

295   passed through an oxidising catalytic converter (a retrofitted diesel oxidation catalyst consisting of a mixture of platinum and rhodium) followed by a standard Volkswagen silencer, then a computer operated pneumatic valve connected to the chamber, with 2 inch bore stainless steel tubing between each component. The whole length of the exhaust line was 4 m. The fuel used was standard UK low sulphur diesel, obtained from a local fuel station.

300   For each run, the engine was started and warmed up at 2000 rpm with 30% load. Once the engine reached a steady temperature (after ~ 10 mins), a controlled amount of the exhaust was injected into the Manchester Aerosol Chamber by switching the valve for a set time (referred this condition as "hot engine"). For the cold start runs (in which no throttle or load was applied, denoted as "cold idle"), the exhaust sample was injected within a minute of the

305   engine starting.

2.1.12 Flame burner

A miniature inverted soot generator (MISG, Argonaut Scientific) operated with propane was used to generate black carbon aerosol. The design, operation, and performance of the MISG hasbeen previously reported (Kazemimanesh et al., 2019;Moallemi et al., 2019). The MISG

310   was operated under two conditions: with the flow rate of propane and air at 0.0625 L min^{-1} and 10 L min^{-1} respectively (Condition 1), and 0.0625 L min^{-1} and 7.5 L min^{-1} respectively

(Condition 2). Under these two conditions, the MISG produces black carbon with average Elemental Carbon/Total Carbon of 95%, determined via thermal-optical analysis.

2.2 Derivation of aerosol dynamic shape factor and material density

315   In this study, the SMPS and CPMA were arranged downstream of the AAC to measure the mobility diameter (D_m) and mass (M_p) of the monodisperse particles selected by the AAC based on their aerodynamic diameter (D_a). These parameters enabled the dynamic shape factor (χ) of the BC particles to be derived by using Eqn. (1) under the assumption that the density (ρ_p) of pure BC is 1.8 g cm^{-3} (DeCarlo et al. (2004)),

320    $$\chi = \frac{D_m C(D_{ve})}{D_{ve} C(D_m)} \qquad (1)$$

in which $C(D)$ is the Cunningham slip correction factor for a particle of diameter D using the parameters specified by (Kim et al., 2005), and D_{ve} is volume equivalent diameter which can be calculated from M_p using Eqn. (2).

$$D_{ve} = \left(\frac{6M_p}{\pi\rho_p}\right)^{\frac{1}{3}} \qquad (2)$$

325   χ can also be determined by using the specified D_a in combination with the SMPS-measured D_m. Specifically, we can calculate D_{ve} from D_a for an initial value of χ_{trial} using Eqn. (3):

$$D_{ve} = D_a \sqrt{\chi \frac{\rho_0}{\rho_p} \frac{C(D_a)}{C(D_{ve})}} \qquad (3)$$

in which ρ_0 is the reference density (1 g cm^{-3}). This value D_{ve} is then substituted into Eqn. (1) to calculate χ. We then iterate through a range of χ_{trial} until χ and χ_{trial} converge.

330   In addition, the material density (ρ_m) of organic aerosols can be calculated from Eqn. (4) and (5) by assuming the organic particles are spherical (i.e., $\chi = 1$) (Adachi et al., 2019).

$$\rho_m = \left(\frac{6M_p}{\pi D_{ve}}\right)^{\frac{1}{3}} \qquad (4)$$

$$D_{ve} = D_m \quad (\text{when } \chi = 1) \qquad (5)$$

2.3 Experimental methods

2.3.1 Wood combustion experiment

Our wood combustion experiments were designed to expand on the studies reported by
Haslett et al. (2018) to produce repeatable combustion events with discernible transitions
between the three burning phases of pyrolysis, flaming, and smouldering combustion. Haslett
et al. (2018) used the FM Global Fire Propagation Apparatus (FPA) (FTT, East Grinstead,
UK) as their controlled ignition source while we used the iCone Calorimeter (Fire Testing
Technology, FTT, East Grinstead, UK) located in the Wildfire laboratory at the University of
Exeter (Fig. 1(a)). The main difference between the FPA and iCone approaches is that the
there is a forced flow of air from beneath the sample in the FPA, whereas in the iCone the
sample sits in ambient air conditions. Otherwise, both approaches rely on oxygen
consumption calorimetry to measure the heat release rate from a burning object.

The aim of the wood combustion experiments was to produce different phases of combustion
that were as well separated as possible, rather than under natural burning conditions. This
allowed the aerosol emissions from different burn phases: pyrolysis, flaming and smouldering,
to be analysed separately. Three core wood types were selected for all the experiments which
we hypothesised would produce different burn conditions, i.e. different durations of pyrolysis,
flaming and smouldering. These wood types were: *Sequioadendron gigantum* (Giant
Redwood), *Pinus sylvestris* (Scots Pine), and *Populus nigra* (Poplar) with bulk densities of
0.45, 0.51, 0.4×10^3 kg/m^3 respectively. The Giant Redwood and Scots Pine are gymnosperm

'softwoods', with the former considered to have low density and the latter a high density,

355 while the Poplar a low density angiosperm 'hard wood' species. In addition we also sampled

combustion emissions from *Thuja plicata* (Western Red Cedar) with a bulk density of 0.38×10^3 kg/m^3. Both Scots pine and Western red cedar are resin rich, while the Giant Redwood

contains less resin, and the Poplar contains barely any resinous compounds. Hence, all should

be capable of producing different volumes and types of aerosol particles. Finally, we assessed

360 wood of two different fuel moistures: fully oven dried samples and moist samples with ~25%

moisture content.

During the experiment, a wood sample (L×W×H (mm): 90×90×30) was first placed into a

custom-made stainless steel basket and then exposed to a radiant heat flux of 40 kW m^{-2}

using the iCone Calorimeter. This radiant heating thermally decomposes the wood sample

365 and generates volatile gases (pyrolysate) as the wood begins to pyrolyse. A spark igniter that

was positioned in the released stream of pyrolysate, igniting the sample once the pyrolysate

reached sufficient concentrations and was well mixed with the surrounding air.

Measurements were taken as soon as a sample was exposed to the radiant heat flux. Each

sample was allowed to flame for 5 minutes and the aerosols captured from this phase and

370 then the flames were snuffed out manually leaving the fuel smouldering so that separate

measurements of the smouldering phase could be taking alone for a further 5 minutes.

Throughout the experiment, the exhaust emissions from combustion were collected in a hood

and entered into an exhaust duct. The concentration of oxygen, carbon dioxide and carbon

monoxide in the exhaust gas were measured by gas analysers integrated into the iCone

375 system and used to calculate the heat release rate from the burning fuel. We installed an

outshoot on this duct to allow part of the exhaust to be carried to a separate sampling system

that allowed the measurement of the aerosol properties in the exhaust. Thus monitoring could

occur in real time by the instruments (described above and shown in Fig. 1), after the exhaust
was diluted with the compressed air through a set of Dekati DI-1000 ejector diluters.

380 Fig. 2 shows an exemplar time series of the rBC and organic aerosol (OA) emitted during
combustion for a representative wood sample. Throughout the wood combustion experiment,
noticeable changes in BC and OA number (and mass) concentration in the exhaust gases were
observed. Following exposure of a wood sample to the heat flux of the iCone and prior to
ignition, a clear signal corresponding to the production of organic aerosols was observed. For

385 these *pyrolysis phase* aerosols, the ratio of the OA mass (M_{OA}, measured by the AMS) to the
sum of masses attributed to OA and rBC (M_{rBC}, measured by SP2, $r_{OA}=M_{OA}/(M_{OA}+M_{rBC})$)
was ~ 1.0, implying that aerosols produced during in the *pyrolysis phase* of combustion was
composed dominantly of organic species. This organic material must be due to the early
stages of pyrolysis where compounds of cellulose and hemicellulose within the wood are

390 being broken down during its thermal decomposition and the surface of the wood begins to
char. We suggest that these pyrolysis phase aerosols are formed from the condensation of
volatile gases into the condensed phase as the aerosol plume lofts upwards away from the
heat source of the iCone and into the cooler environment of the exhaust system.

Immediately after ignition, the number (and mass) concentration of the OA decreased

395 abruptly, while the rBC mass concentration increased sharply to 150 μg/m³ (Fig. 2). We refer
to this combustion phase following ignition as the *flaming phase*. The r_{OA} at the onset of
flaming combustion (the first 90s after ignition) is less than 0.05, indicating that most of the
emitted aerosols during this period are BC. As flaming combustion progressed, the extent and
depth of charring increased and as the flammable gas flux slows the flame begins to diminish.

400 Char is a strong insulator and hence the char layer forms an obstacle to the conduction of heat
into the lower uncharred layers wood, reducing the production rate of the flammable gases

and decreasing the rate of heat release from combustion. As flaming subsides the number (and mass) concentration of BC particles decreases (Fig. 2) and the r_{OA} increased to around 0.2 after 300 s of the ignition.

405 After ~300 s (5 min) from the time of ignition the flames were snuffed manually to force the combustion from the flaming to the smouldering phase, thus transitioning the oxidation reaction from that on gas phase species to direct oxidation of the solid fuel. Fig. 2 shows that the number (and mass) concentration of rBC in the *smouldering phase* decreased abruptly as flaming combustion ceased and the OA concentration increased sharply. The r_{OA} was 1.0

410 during this period, indicating that almost all the emitted aerosols are composed of organic species only.

2.3.2 SP2 incandescence signal calibration and BC morphology investigation experiment

For the purposes of SP2 incandescence signal calibration and morphology investigation of BC particles, three types of the BC particles other than that emitted from wood combustion

415 were investigated through chamber experiments (Fig. 1(b)). For the BC particles generated by the MISG: BC particles were introduced into the chamber through a Dekati DI-1000 ejector diluter. For the BC particles from the Aquadag standards: the Aquadag standards was first generated by an aerosol atomizer (Topas ATM 226) and then passed through a diffusion drier (using silica dessicant) prior to entering the chamber. For the BC particles emitted from the

420 engine: a hot engine running condition (2,000 r.p.m., 30% load and 10 min warm up) and a cold idle condition were investigated. After the BC mass concentration had accumulated to adequate levels in the chamber, a catalytic stripper (operated at 350°C, Model CS10, Catalytic Instruments, Germany) was used to remove the coatings on the BC particles before they were sampled by the instruments.

2.3.3 SOA formation through chamber experiments

For the purpose of testing models of BC and SOA mixing during the SASSO project, two procedures for generating SOA were used: one that yielded non-absorbing SOA and one that produced brown carbon. Experiments were conducted in the photochemical aerosol reaction chamber at the University of Manchester. During the experiment, NO_2 was injected directly into the bag from a cylinder via stainless steel tubing, and its concentration was measured using a chemo-luminescence gas analyzer (Model 42i, Thermo Scientific, MA, USA). After the NO_x concentration in the bag reached the desirable value, the precursor VOC was injected into a heated glass bulb (80°C) and flushed into the bag with high purity nitrogen. Subsequently, chamber lights were turned on to trigger SOA formation. The EXSCALABAR system was used to determine the light absorption properties of the formed SOA particles in real time throughout the experiment.

In this study, 50 ppb NO_x and 250 ppb α-pinene (Sigma-Aldrich) was used to form non-absorbing SOA; this route to forming non-absorbing SOA is well characterized and has been reported previously (Nakayama et al., 2010). Here, we only focus on the methodology used to produce the brown carbon SOA. Previous work has reported 'brown' SOA formation through oxidation of aromatic precursors under high NO_x conditions (Laskin et al., 2015). In this study, we injected ~ 400 ppb cresol (Sigma-Aldrich) and ~ 15 ppb NO_2 (~ 60 ppb NO_x in the chamber) into the chamber, and removed the UV filter from one of the Xenon arc lamps to accelerate and enhance the 'brown' SOA formation. As shown in Fig. 3, after the precursors were introduced into the chamber and the lights were switched on, the SOA started to form and the particle size increased to ~ 200 nm after 40 minutes. Over this same time period, we measured increasing aerosol absorption and extinction coefficients, the single scattering albedo (SSA) was observed to increase sharply at the onset of the SOA formation

and then stabilized at around 0.81 (at 405 nm) eventually. Most of the evolution in SSA (i.e.

450   increasing over time) is expected to be caused by the increase in particle size over a size

range where SSA is very sensitive to particle size. We emphasise that we did not inject any

primary ozone in this experiment, and the abrupt increase in ozone concentration around the

time of VOC injection is caused by UV photochemistry involving the light absorption of

cresol. In addition, we highlight that we only present aerosol optical data here to demonstrate

455   brown carbon formation, while a comprehensive analysis of our optical data is the subject of

a future publication.

2.3.4 BC restructuring experiment

Recent work has shown that soot particles maintain their structure after coating with SOA

and subsequent thermal denuding (Bhandari et al., 2017), but will restructure in response to

460   humidification (Leung et al., 2017). We performed a series of experiments to better

understand this restructuring. First, bare BC particles with minimal accompanying VOCs

were injected into the chamber by using an oxidising catalytic converter, heated ejector

dilutors, a catalytic stripper, Purafil, and activated charcoal denuders between the exhaust line

of the engine and the chamber inlet. After the BC reached the desirable concentration, BC

465   injection was stopped. The particle size distribution of the dried bare BC particles was

scanned by the AAC. In addition, the particle size distribution of the dried bare BC particles

following 'humidity cycling', i.e. exposure to 90% RH for around 10 s and then dehydration

to 10% RH, was measured by AAC for comparison. Afterwards, we injected 50 ppb NO_x and

250 ppb α-pinene into the chamber. Photochemical reaction was initiated by turning the

470   chamber lights on, and organic materials condense onto the BC particulates. After the

condensed organics equilibrate with the surrounding VOCs and the particles stabilised at a

certain size, the aerodynamic particle size distribution of the dried organic coated BC

particles, and that of the dried organic coated BC particles experienced the humidity cycling, was measured by AAC. As shown in Fig. 4, there is no clear change in particle size for the

475 dried bare BC after they experience the humidity cycling process, implying that the bare BC particles retain their structure even after they experience very large perturbations in RH. In addition, no size change of the organic coated BC particles was observed after they experienced the humidity cycling process either. Based on these results, we cannot form conclusions on whether the BC core was restructured during the humidity cycling process.

480 There are two possibilities: (1) The BC cores retained their structure throughout humidity cycling process; or (2) The BC cores were restructured during the humidity cycling process, but any changes were not reflected by changes in the overall particle size as this was mainly dominated/contributed by the coating organics. To further examine these possibilities, the organic coatings of the coated BC particles, that had either experienced the humidity cycling

485 process or not, were removed by the TD, and then the size distribution of the BC core was measured by the AAC and SMPS. As shown in Fig. 5, a clear difference in BC core size was observed between the organic coated BC particles that had passed immediately through the TD (Fig. 5(a)) and those that had first experienced the humidity cycling process (Fig. 5(b)). The mobility diameter of the BC core size peaked at 79.3 nm for the former case but peaked

490 at 23.6 nm for the latter one, implying that the BC core was restructured (becomes more compact) after coating with organics and then experiencing the high humidity environment.

3 Results and Discussion

3.1 SP2 incandescence signal calibration with different types of BC particles

The conventional way to calibrate the incandescence channel of SP2 is using monodisperse

495 Aquadag standards (Acheson Inc. USA), which is then corrected for ambient rBC by applying a constant factor of 0.75 based on a previous laboratory comparison (Laborde et al.,

2012b). As the incandescence signal is not independent for the different types of BC particles, using a constant factor of 0.75 may introduce large uncertainty in the retrieved BC mass concentration. Thus, quantifying the correction factor for many types of BC particles found

500 commonly in the atmosphere may enable better constraints to be placed on this factor depending on the BC source being sampled, thus improve the accuracy of future SP2 measurements of rBC mass concentrations. The broad range of BC aerosols generated in this study from different combustion sources served as an ideal platform to assess the variation in this correction factor to SP2-derived rBC mass.

505 In this study, the incandescence signal of the SP2 was measured for BC particles from catalytically stripped diesel engine exhaust emissions, a flame burner, and controlled flaming wood combustion, respectively, and compared with that measured from an Aquadag standard. As shown in Fig. 6, for the BC particles emitted from the diesel engine under hot engine and cold idle conditions (Fig. 6(a)), the slopes of the incandescence signal with BC mass are 0.82

510 and 0.79 times of that measured from the Aquadag standard, respectively. These correction factors are 9.3% and 5.3% different with the common value of 0.75 (with the uncertainty less than 5%) recommended by Laborde et al. (2012b) when deriving the mass concentration of BC emitted from diesel engines. For the BC particles generated from the flame burner (Fig. 6(b)), the correction factor is 0.88. Meanwhile, for the BC particles emitted from the flaming

515 phase during the combustion of Scots pine, Poplar, Giant Redwood or Western red cedar, the correction factors are 0.91, 0.91, 0.89 or 0.84, respectively. We stress that, for the SP2 calibrations here from wood combustion emissions, the BC particles were not treated with a catalytic stripper before sampling by the SP2. However, as shown in Fig. 2(c), the BC particles generated at the beginning of the flaming phase contained almost no organic species,

520 with r_{OA} values less than 0.05 and the coating thicknesses calculated from SP2 data were around 1.01.

The differences in the correction factors derived in this study with the default value of 0.75 are 9.3% (5.3%), 17.3% and 12.0-21.3% for the BC particles emitted from engine with hot engine (or cold idle) condition, flame burner and wood combustion, respectively. We

525 recommend that future studies utilizing the SP2 for rBC mass concentration measurements use SP2 calibrations with the same type of BC as that to be studied.

3.2 Physical properties of black carbon and organic aerosols

The morphology of BC particles change markedly during atmospheric aging, with associated impacts on the particle size and optical properties (Zeng et al., 2019;Zhang et al., 2008;Teoh

530 et al., 2019). In this study, the dynamic shape factor of BC particles and the material density of organic aerosols were derived by measuring the mass and/or mobility diameter of AAC-selected particles. For biomass burning aerosols generated through our controlled combustion of dry wood samples, the AAC was set to pass aerosols with an aerodynamic diameter D_a=200 nm and we sampled BC or organic aerosols produced from the flaming or

535 smouldering phases, respectively. Number concentration measurements from the CPC were recorded as the CPMA was scanned to determine the aerosol mass distribution. Figure 7(a) shows that there are considerable differences in the mass distributions for the produced BC (during the flaming phase) and organic aerosols (during the smouldering phase). The peak mass of BC particles produced from the wood samples of the Scots pine, Poplar and Giant

540 Redwood are 10.86, 12.47 and 7.00 fg, respectively. Meanwhile, the corresponding peak mass for the organic aerosols are 1.72, 1.74 and 1.90 fg, respectively. This difference is likely due to the difference in density and morphology for BC and organic aerosols. BC normally has a large density and a more irregular morphology than organic aerosols. After the peak

masses for the AAC-selected aerosols were ascertained, the CPMA was set to these values to

545   further select the AAC-selected aerosols (D_a=200 nm) by their peak mass for a subsequent

mobility size measurement using our SMPS. Figure 7(b) shows that the corresponding peak

mobility size of the monodisperse BC and organic particles are 394, 405, 292 nm and 139,

139, 140 nm for Scots pine, Poplar and Giant Redwood, respectively. From these

aforementioned peak mobility diameters and aerosol masses, the χ of the BC particles and the

550   ρ_m of the organics can be calculated from the methods described in Sect. 2.2. We highlight

the discussion in Sect. 2.2 that stated that χ could be calculated using either the aerodynamic

or volume-equivalent diameter; as organic species may evaporate during the AAC selection

(due to the high sheath flow rate) and thus bias the D_a, only the mass and mobility size

distributions were used in these calculations. Table 1 summarises the χ values inferred for the

555   D_a=200 nm BC particles, with values of 2.17, 2.10 and 1.80 ascertained for oven dried

samples of Scots pine, Poplar and Giant Redwood, respectively. The ρ_m of the organics are

1.22, 1.23 and 1.32 g/cm^3 for oven dried samples of Scots pine, Poplar and Giant Redwood,

respectively. For combustion experiments using wet wood samples (with moisture contents

around 25%), the CPMA instrument was unavailable. Instead, the mobility size distributions

560   for the AAC-selected D_a=200 nm BC particles or organic particles were measured by the

SMPS immediately after AAC-selection. As shown in Fig. 8, the peak mobility size of the

BC and organic particles are 296, 256, 161 nm and 149, 142, 137 nm for Scots pine, Poplar

and Giant Redwood, respectively. Based on their aerodynamic and mobility size, the χ of the

BC particles and the ρ_m of the organics were calculated and summarised in Table 1. The χ of

565   the D_a=200 nm BC particles are 1.85, 1.67 and 1.20 for Scots pine, Poplar and Giant

Redwood, respectively, lower than that of the dry wood samples. The ρ_m of the organics are

1.44, 1.52 and 1.60 g/cm^3 for Scots pine, Poplar and Giant Redwood, respectively, higher

than that of the dry wood samples. This result implies that the water contents of wood samples are important in determining the physical properties of emitted particles from their

570 combustion. The densities of organic aerosols reported/used in previous studies vary significantly, from 0.6 to 1.4 g cm^{-3} (Turpin and Lim, 2001;Nakao et al., 2013;Li et al., 2016). For the biomass burning aerosols, Zhai et al. (2017) reported the effective density ranged from 1.35 to 1.51 g cm^{-3} for the carbonaceous aerosol produced from the agricultural residue burning. Our results would expand the available data on the variation densities for organic

575 aerosols from the wood combustion.

For the BC particles from the catalytically stripped Aquadag standard, diesel engine exhaust, and flame burner, particles were first selected by the AAC prior to mobility size distribution measurements using the SMPS. The χ of the BC particles were derived from the controlled aerodynamic size and the measured peak mobility diameter. Fig. 9(a) shows that the particle

580 mobility diameter increases with the selected aerodynamic size for all three types of BC particles, while Fig. 9(b) shows the corresponding variations in χ. These figures demonstrate clearly that the dynamic shape factor varies with both the aerosol aerodynamic size and with the BC source. For the BC particles generated from the Aquadag standard, the χ increased sharply from 1.32 to 1.46 as D_a increased from 75 nm to 125 nm, but then decreased with

585 further increases in D_a to a value of 1.25 at D_a=500 nm. This result implies that the formed BC particles are more irregular as D_a increases initially, but particles adopt more collapsed morphologies as D_a increases further. These trends in χ likely arise from the coagulation of the primary BC particles, which drives the fractal-like morphology for small BC particles and relative compact shape for large particles. For BC particles generated from the diesel engine,

590 the χ exhibits a monotonically decreasing trend with particle size over the reduced size range probed for this BC source, with χ decreasing from 1.33 at D_a=150 nm to 1.24 at D_a=275 nm.

The TEM images (Fig. 9(c)) show that the primary spherules generated directly from the diesel engine are around 20 nm. As the BC particles selected in the experiment are much larger than the primary spherules, the coagulation process drives the large particles towards

595   more compacted morphologies than the small particles and this leads to the decreasing trend of χ with particle size. For the BC particles generated from the flame burner, the χ increases with particle size for both operating conditions and a maximum value was reached of 2.73 for $D_a = 150$ nm. The same increasing trend was reported by Slowik et al. (2004) previously, who reported an increase in χ from ~ 1.3 to ~ 3.0 when the mobility size increased from 100

600   nm to 300 nm for the BC particles generated with lower propane/O_2 ratio compared to the measurements we report here. The TEM images (Fig. 9(d)) shows that, similar to the BC particles emitted from diesel engine, the primary spherules generated from the flame burner are also around 20 nm. As our experiments on BC particles from the flame burner selected particles at small sizes (D_a in the range ~ 50 – 150 nm), the increase of the dynamic shape

605   factor with D_a is probably due to the coagulation of primary generated particles. In addition, by comparing Fig. 9(c) and Fig. 9(d) (more images are shown in Fig. S1), it is clear that the large BC particles generated from the flame burner tend towards aggregate morphology, in contrast to the compact morphology of the large BC particles emitted from the diesel engine (Fig. 9(c)). This leads to the flame burner generated BC particles exhibiting larger χ than

610   those from the diesel engine.

3.3 AMS Mass spectra of organic aerosols

Owing to the complex nature of biomass combustion in the natural environment, and the high sensitivity to the combustion environment, the organic mass spectral signatures from previous AMS experiments vary considerably. This variability makes it difficult to estimate the

615   contribution of biomass burning aerosol (BBA) to total PM through positive matrix

factorisation (PMF) methods (Paglione et al., 2020). The mass spectra for the BBA generated from our repeatable and controlled laboratory experiments have the potential to tighten constraints on the AMS spectral signature for BBA. Highly controlled and reproducible measurements of aerosol emissions from combustion of a common African biofuel source has

620 been achieved and reported by Haslett et al. (2018) previously. Here, we expand detail of the mass spectra observations reported by Haslett et al. (2018) by providing data sets on the combustion for different types of biomass to that studied in previous work.

The mass spectra of organic aerosols generated from the pyrolysis and smouldering phases, and the difference mass spectra between these two phases, are shown in Fig. 10 and Fig. 11

625 for the combustion of dry and wet wood samples, respectively. For all experiments, irrespective of the wood type and moisture content, the spectra for the pyrolysis and smouldering phases are dominated by hydrocarbon ion fragments, including C_nH_{2n-1} (m/z=41, 55), C_nH_{2n+1} (m/z=29, 43, 57), C_nH_{2n-3} (m/z=67) and $C_{5+n}H_{5+2n}$ (m/z=77, 91). These peaks are associated with fragments of saturated alkenes, alkanes, cycloalkanes and aromatic

630 compounds, respectively. Our results are similar to the mass spectra reported by Haslett et al. (2018) for the controlled combustion of biomass in the laboratory. By comparing Fig. 10 and Fig. 11, no clear difference in mass spectra of the organic aerosols in individual burn phases (pyrolysis or smouldering phase) with the moisture content of the wood samples are observed. This implies that the effect moisture has on the organic chemical profile of wood burning

635 emissions is through changing the durations of the different phases of the burn cycle, not through the chemical modification of the individual phases. This is in stark contrast to the dominant role of the wood water content in determining the morphological parameters and densities of generated biomass burning aerosols shown in Sect. 3.2.

The peaks at m/z 57, 60 and 73 are seen together in both combustion phases; these peaks are

640   often used as markers for biomass burning organic aerosols (Alfarra et al., 2007), as very few

other aerosol sources in the natural environment can contribute to these peaks. Interestingly,

for the wood samples of Scots pine, Giant Redwood and Western red cedar, these peaks at

m/z 57, 60 and 73 were more dominant in the pyrolysis phase. This is a similar observation to

that reported by Haslett et al. (2018). However, for the Poplar wood sample, the peaks are

645   most dominated in the smouldering phase. This is particularly interesting because it suggests

that the combustion of angiosperm wood (Poplar) and gymnosperm wood (Scots Pine, Giant

Redwood and Western red cedar) will emit different chemical species depending on the

combustion phase. This difference may be due to the resin content and composition (which is

related to chemical volatility) within the wood. Future work should consider the impact of

650   burning of different wood types and their respective relationship to combustion phase.

For all wood samples, the peak at m/z 44, which is mainly attributed to the CO_2^+ fragment

with a possible contribution from $C_2H_4O^+$, is more prominent in pyrolysis phase than the

smouldering phase, which is contrast with the results from Haslett et al. (2018). This could be

a result of the different wood types. We note that the study of Haslett et al., (2018) used

655   Rubber wood (*Hevea brasiliensis*), that produces latex sap. This hard tropical wood also has a

bulk density much higher than the woods tested here (0.63 x 10^3 kg/m^3) and likely a higher

lignin content where lignin is one the last compounds to be broken down by the combustion

process.

4 Conclusions

660   During the Soot Aerodynamic Size Selection for Optical properties (SASSO) project and a

EUROCHAMP transnational access project, the physical and chemical properties of black

carbon and organic matter from different combustion sources were investigated. For BC

particles from the diesel engine and flame burner emissions, the TEM images show that the primary spherules size are similar, around 20 nm. As particle size increases, BC particles

665 adopted more collapsed/compacted morphologies from the diesel engine but tend to more aggregated morphologies from the flame burner source. For the particles emitted from the wood combustion, the χ of BC particles and the ρ_m of organics were observed to range from 1.8-2.17 and 1.22-1.32 g/cm^3 for dry wood samples, 1.2-1.85 and 1.44-1.60 g/cm^3 for wet wood samples. No clear difference in the AMS mass spectra of the organic aerosols in

670 individual burn phases (pyrolysis or smouldering phase) with the moisture content of the wood samples were observed. This implies that the effect moisture has on the organic chemical profile of wood burning emissions is through changing the durations of the different phases of the burn cycle, not through the chemical modification of the individual phases. In addition, the incandescence signal of SP2 was calibrated with the different types of BC

675 particles generated in our study and compared that with the Aquadag standard. The correction factor, which is used for converting the incandescence signal from the Aquadag standard to the investigated BC, was measured as 0.82 (or 0.79), 0.88 and 0.84-0.91 for the BC particles emitted from engine under hot running (or cold idle) condition, flame burner and wood combustion, respectively. These values are 9.3% (5.3%), 17.3% and 12.0-21.3% different

680 with the default value of 0.75 used recently. Quantifying the correction factor for many types of BC particles found commonly in the atmosphere may enable better constraints to be placed on this factor depending on the BC source being sampled, and thus improve the accuracy of future SP2 measurements of rBC mass concentrations.

Acknowledgements

685 This work was supported by the UK Natural Environment Research Council (NERC) (grant ref. NE/S00212X/1) and the Met Office, and received a trans-national activity funding from

the European Union's Horizon 2020 research and innovation programme through the EUROCHAMP-2020 Infrastructure Activity under grant agreement No. 730997. Prem Lobo was supported by the UK National Centre for Atmospheric Science (NCAS) Visiting

690   Scientist Programme. Thanks to Catalytic Instruments for the loan of the catalytic stripper CS10, and to Xioamei Du for at National Research Council Canada for the TEM images.

Author contributions. D.A., D.H., R.A. D.L. J.H. and H.C. designed research; D.H., C.Y., R.A., K.S., J.L., M.C., C.B., I.R. and Z.L. performed wood combustion experiments; D.H., R.A., Y.S., M.D. and A.V. performed Manchester aerosol chamber experiments; B.S., P.L.

695   and G.S. performed the burner experiments. D.H. conducted the data analysis and wrote the manuscript with inputs from all co-authors.

Data availability. Raw data is archived at the University of Manchester and is available on request.

Competing financial interests

700   The authors declare no competing financial interests.

Reference

Adachi, K., Sedlacek, A. J., Kleinman, L., Springston, S. R., Wang, J., Chand, D., et al., 2019. Spherical tarball particles form through rapid chemical and physical changes of organic matter in biomass-burning smoke. Proceedings of the National Academy of Sciences. 116,

705   19336-19341.

Alfarra, M. R., Hamilton, J. F., Wyche, K. P., Good, N., Ward, M. W., Carr, T., et al., 2012. The effect of photochemical ageing and initial precursor concentration on the composition and hygroscopic properties of β-caryophyllene secondary organic aerosol. Atmos. Chem. Phys. 12, 6417-6436.

710   Alfarra, M. R., Prevot, A. S. H., Szidat, S., Sandradewi, J., Weimer, S., Lanz, V. A., et al.,
      2007. Identification of the Mass Spectral Signature of Organic Aerosols from Wood Burning
      Emissions. Environmental Science & Technology. 41, 5770-5777.

      Andreae, M. O., and Crutzen, P. J., 1997. Atmospheric Aerosols: Biogeochemical Sources
      and Role in Atmospheric Chemistry. Science. 276, 1052-1058.

715   Bhandari, J., China, S., Onasch, T., Wolff, L., Lambe, A., Davidovits, P., et al., 2017. Effect
      of Thermodenuding on the Structure of Nascent Flame Soot Aggregates. Atmosphere. 8, 166.

      Bond, T. C., 2001. Spectral dependence of visible light absorption by carbonaceous particles
      emitted from coal combustion. Geophysical Research Letters. 28, 4075-4078.

      Bond, T. C., and Bergstrom, R. W., 2006. Light absorption by carbonaceous particles: An
720   investigative review. Aerosol Sci. Tech. 40, 27-67.

      Bond, T. C., Doherty, S. J., Fahey, D. W., Forster, P. M., Berntsen, T., DeAngelo, B. J., et al.,
      2013. Bounding the role of black carbon in the climate system: A scientific assessment.
      Journal of Geophysical Research: Atmospheres. 118, 5380-5552.

      Bones, D. L., Henricksen, D. K., Mang, S. A., Gonsior, M., Bateman, A. P., Nguyen, T. B., et
725   al., 2010. Appearance of strong absorbers and fluorophores in limonene-O3 secondary
      organic aerosol due to NH4+-mediated chemical aging over long time scales. Journal of
      Geophysical Research: Atmospheres. 115.

      Corbin, J. C., Czech, H., Massabò, D., de Mongeot, F. B., Jakobi, G., Liu, F., et al., 2019.
      Infrared-absorbing carbonaceous tar can dominate light absorption by marine-engine exhaust.
730   npj Climate and Atmospheric Science. 2, 12.

      Cotterell, M. I., Orr-Ewing, A. J., Szpek, K., Haywood, J. M., and Langridge, J. M., 2019a.
      The impact of bath gas composition on the calibration of photoacoustic spectrometers with
      ozone at discrete visible wavelengths spanning the Chappuis band. Atmos. Meas. Tech. 12,
      2371-2385.

735 Cotterell, M. I., Szpek, K., Haywood, J. M., and Langridge, J. M., 2020. Sensitivity and accuracy of refractive index retrievals from measured extinction and absorption cross sections for mobility-selected internally mixed light absorbing aerosols. Aerosol Science and Technology. 54, 1034-1057.

Cotterell, M. I., Ward, G. P., Hibbins, A. P., Wilson, A., Haywood, J. M., and Langridge, J.
740 M., 2019b. Optimizing the performance of aerosol photoacoustic cells using a finite element model. Part 2: Application to a two-resonator cell. Aerosol Science and Technology. 53, 1128-1148.

Davies, N. W., Cotterell, M. I., Fox, C., Szpek, K., Haywood, J. M., and Langridge, J. M., 2018. On the accuracy of aerosol photoacoustic spectrometer calibrations using absorption by
745 ozone. Atmos. Meas. Tech. 11, 2313-2324.

De Haan, D. O., Hawkins, L. N., Welsh, H. G., Pednekar, R., Casar, J. R., Pennington, E. A., et al., 2017. Brown Carbon Production in Ammonium- or Amine-Containing Aerosol Particles by Reactive Uptake of Methylglyoxal and Photolytic Cloud Cycling. Environmental Science & Technology. 51, 7458-7466.

750 DeCarlo, P. F., Slowik, J. G., Worsnop, D. R., Davidovits, P., and Jimenez, J. L., 2004. Particle Morphology and Density Characterization by Combined Mobility and Aerodynamic Diameter Measurements. Part 1: Theory. Aerosol Science and Technology. 38, 1185-1205.

Gao, R. S., Schwarz, J. P., Kelly, K. K., Fahey, D. W., Watts, L. A., Thompson, T. L., et al., 2007. A Novel Method for Estimating Light-Scattering Properties of Soot Aerosols Using a
755 Modified Single-Particle Soot Photometer. Aerosol Science and Technology. 41, 125-135.

Good, N., Coe, H., and McFiggans, G., 2010. Instrumentational operation and analytical methodology for the reconciliation of aerosol water uptake under sub- and supersaturated conditions. Atmos. Meas. Tech. . 3, 1241-1254.

Harrison, M. A. J., Barra, S., Borghesi, D., Vione, D., Arsene, C., and Iulian Olariu, R., 2005.

760   Nitrated phenols in the atmosphere: a review. Atmospheric Environment. 39, 231-248.

Haslett, S. L., Thomas, J. C., Morgan, W. T., Hadden, R., Liu, D., Allan, J. D., et al., 2018.

Highly controlled, reproducible measurements of aerosol emissions from combustion of

a common African biofuel source. Atmos. Chem. Phys. 18, 385-403.

Haywood, J. M., and Shine, K. P., 1995. The effect of anthropogenic sulfate and soot aerosol

765   on the clear sky planetary radiation budget. Geophysical Research Letters. 22, 603-606.

Jayne, J. T., Leard, D. C., Zhang, X., Davidovits, P., Smith, K. A., Kolb, C. E., et al., 2000.

Development of an Aerosol Mass Spectrometer for Size and Composition Analysis of

Submicron Particles. Aerosol Science and Technology. 33, 49-70.

Kazemimanesh, M., Moallemi, A., Thomson, K., Smallwood, G., Lobo, P., and Olfert, J. S.,

770   2019. A novel miniature inverted-flame burner for the generation of soot nanoparticles.

Aerosol Science and Technology. 53, 184-195.

Kim, J. H., Mulholland, G. W., Kukuck, S. R., and Pui, D. Y., 2005. Slip Correction

Measurements of Certified PSL Nanoparticles Using a Nanometer Differential Mobility

Analyzer (Nano-DMA) for Knudsen Number From 0.5 to 83. Journal of research of the

775   National Institute of Standards and Technology. 110, 31-54.

Kirchstetter, T. W., Novakov, T., and Hobbs, P. V., 2004. Evidence that the spectral

dependence of light absorption by aerosols is affected by organic carbon. Journal of

Geophysical Research: Atmospheres. 109.

Laborde, M., Mertes, P., Zieger, P., Dommen, J., Baltensperger, U., and Gysel, M., 2012a.

780   Sensitivity of the Single Particle Soot Photometer to different black carbon types. Atmos.

Meas. Tech. 5, 1031-1043.

Laborde, M., Schnaiter, M., Linke, C., Saathoff, H., Naumann, K. H., Möhler, O., et al., 2012b. Single Particle Soot Photometer intercomparison at the AIDA chamber. Atmos. Meas. Tech. 5, 3077-3097.

785 Laskin, A., Laskin, J., and Nizkorodov, S. A., 2015. Chemistry of Atmospheric Brown Carbon. Chemical Reviews. 115, 4335-4382.

Leung, K. K., Schnitzler, E. G., Jäger, W., and Olfert, J. S., 2017. Relative Humidity Dependence of Soot Aggregate Restructuring Induced by Secondary Organic Aerosol: Effects of Water on Coating Viscosity and Surface Tension. Environmental Science & 790 Technology Letters. 4, 386-390.

Li, C., Hu, Y., Chen, J., Ma, Z., Ye, X., Yang, X., et al., 2016. Physiochemical properties of carbonaceous aerosol from agricultural residue burning: Density, volatility, and hygroscopicity. Atmospheric Environment. 140, 94-105.

Lin, P., Liu, J., Shilling, J. E., Kathmann, S. M., Laskin, J., and Laskin, A., 2015. Molecular 795 characterization of brown carbon (BrC) chromophores in secondary organic aerosol generated from photo-oxidation of toluene. Physical Chemistry Chemical Physics. 17, 23312-23325.

Liu, D., Allan, J. D., Young, D. E., Coe, H., Beddows, D., Fleming, Z. L., et al., 2014. Size distribution, mixing state and source apportionment of black carbon aerosol in London during 800 wintertime. Atmos. Chem. Phys. 14, 10061-10084.

Liu, D., Flynn, M., Gysel, M., Targino, A., Crawford, I., Bower, K., et al., 2010. Single particle characterization of black carbon aerosols at a tropospheric alpine site in Switzerland. Atmos. Chem. Phys. 10, 7389-7407.

Liu, D., He, C., Schwarz, J. P., and Wang, X., 2020a. Lifecycle of light-absorbing 805 carbonaceous aerosols in the atmosphere. npj Climate and Atmospheric Science. 3, 40.

Liu, D., Whitehead, J., Alfarra, M. R., Reyes-Villegas, E., Spracklen, Dominick V., Reddington, Carly L., et al., 2017. Black-carbon absorption enhancement in the atmosphere determined by particle mixing state. Nature Geoscience. 10, 184-188.

Liu, F., Yon, J., Fuentes, A., Lobo, P., Smallwood, G. J., and Corbin, J. C., 2020b. Review of recent literature on the light absorption properties of black carbon: Refractive index, mass absorption cross section, and absorption function. Aerosol Science and Technology. 54, 33-51.

Lu, J. W., Flores, J. M., Lavi, A., Abo-Riziq, A., and Rudich, Y., 2011. Changes in the optical properties of benzo[a]pyrene-coated aerosols upon heterogeneous reactions with NO2 and NO3. Physical Chemistry Chemical Physics. 13, 6484-6492.

Maxut, A., Nozière, B., Fenet, B., and Mechakra, H., 2015. Formation mechanisms and yields of small imidazoles from reactions of glyoxal with NH4+ in water at neutral pH. Physical Chemistry Chemical Physics. 17, 20416-20424.

Miles, R. E. H., Rudić, S., Orr-Ewing, A. J., and Reid, J. P., 2011. Sources of Error and Uncertainty in the Use of Cavity Ring Down Spectroscopy to Measure Aerosol Optical Properties. Aerosol Science and Technology. 45, 1360-1375.

Miller, A., Frey, G., King, G., and Sunderman, C., 2010. A Handheld Electrostatic Precipitator for Sampling Airborne Particles and Nanoparticles. Aerosol Science and Technology. 44, 417-427.

Moallemi, A., Kazemimanesh, M., Corbin, J. C., Thomson, K., Smallwood, G., Olfert, J. S., et al., 2019. Characterization of black carbon particles generated by a propane-fueled miniature inverted soot generator. Journal of Aerosol Science. 135, 46-57.

Nakao, S., Tang, P., Tang, X., Clark, C. H., Qi, L., Seo, E., et al., 2013. Density and elemental ratios of secondary organic aerosol: Application of a density prediction method. Atmospheric Environment. 68, 273-277.

Nakayama, T., Matsumi, Y., Sato, K., Imamura, T., Yamazaki, A., and Uchiyama, A., 2010. Laboratory studies on optical properties of secondary organic aerosols generated during the photooxidation of toluene and the ozonolysis of α-pinene. Journal of Geophysical Research: Atmospheres. 115.

835   Noziere, B., and Esteve, W., 2007. Light-absorbing aldol condensation products in acidic aerosols: Spectra, kinetics, and contribution to the absorption index. Atmospheric Environment. 41, 1150-1163.

Olfert, J. S., and Collings, N., 2005. New method for particle mass classification—the Couette centrifugal particle mass analyzer. Journal of Aerosol Science. 36, 1338-1352.

840   Olfert, J. S., Reavell, K. S., Rushton, M. G., and Collings, N., 2006. The experimental transfer function of the Couette centrifugal particle mass analyzer. Journal of Aerosol Science. 37, 1840-1852.

Paglione, M., Gilardoni, S., Rinaldi, M., Decesari, S., Zanca, N., Sandrini, S., et al., 2020. The impact of biomass burning and aqueous-phase processing on air quality: a multi-year

845   source apportionment study in the Po Valley, Italy. Atmos. Chem. Phys. 20, 1233-1254.

Powelson, M. H., Espelien, B. M., Hawkins, L. N., Galloway, M. M., and De Haan, D. O., 2014. Brown Carbon Formation by Aqueous-Phase Carbonyl Compound Reactions with Amines and Ammonium Sulfate. Environmental Science & Technology. 48, 985-993.

Ramanathan, V., Li, F., Ramana, M. V., Praveen, P. S., Kim, D., Corrigan, C. E., et al., 2007.

850   Atmospheric brown clouds: Hemispherical and regional variations in long-range transport, absorption, and radiative forcing. Journal of Geophysical Research: Atmospheres. 112.

Shapiro, E. L., Szprengiel, J., Sareen, N., Jen, C. N., Giordano, M. R., and McNeill, V. F., 2009. Light-absorbing secondary organic material formed by glyoxal in aqueous aerosol mimics. Atmos. Chem. Phys. 9, 2289-2300.

855   Slowik, J. G., Stainken, K., Davidovits, P., Williams, L. R., Jayne, J. T., Kolb, C. E., et al., 2004. Particle Morphology and Density Characterization by Combined Mobility and Aerodynamic Diameter Measurements. Part 2: Application to Combustion-Generated Soot Aerosols as a Function of Fuel Equivalence Ratio. Aerosol Science and Technology. 38, 1206-1222.

860   Tavakoli, F., Symonds, J. P. R., and Olfert, J. S., 2014. Generation of a Monodisperse Size-Classified Aerosol Independent of Particle Charge. Aerosol Science and Technology. 48, i-iv.

Taylor, J. W., Wu, H., Szpek, K., Bower, K., Crawford, I., Flynn, M. J., et al., 2020. Absorption closure in highly aged biomass burning smoke. Atmos. Chem. Phys. 20, 11201-11221.

865   Teoh, R., Stettler, M. E. J., Majumdar, A., Schumann, U., Graves, B., and Boies, A. M., 2019. A methodology to relate black carbon particle number and mass emissions. Journal of Aerosol Science. 132, 44-59.

Turpin, B. J., and Lim, H.-J., 2001. Species Contributions to PM2.5 Mass Concentrations: Revisiting Common Assumptions for Estimating Organic Mass. Aerosol Science and
870   Technology. 35, 602-610.

Voliotis, A., Prokeš, R., Lammel, G., and Samara, C., 2017. New insights on humic-like substances associated with wintertime urban aerosols from central and southern Europe: Size-resolved chemical characterization and optical properties. Atmospheric Environment. 166, 286-299.

875   Voliotis, A., Wang, Y., Shao, Y., Du, M., Bannan, T. J., Percival, C. J., et al., 2021. Exploring the composition and volatility of secondary organic aerosols in mixed anthropogenic and biogenic precursor systems. Atmos. Chem. Phys. Discuss. 2021, 1-39.

Zarzana, K. J., Cappa, C. D., and Tolbert, M. A., 2014. Sensitivity of Aerosol Refractive Index Retrievals Using Optical Spectroscopy. Aerosol Science and Technology. 48, 1133-1144.

Zeng, C., Liu, C., Li, J., Zhu, B., Yin, Y., and Wang, Y., 2019. Optical Properties and Radiative Forcing of Aged BC due to Hygroscopic Growth: Effects of the Aggregate Structure. Journal of Geophysical Research: Atmospheres. 124, 4620-4633.

Zhai, J., Lu, X., Li, L., Zhang, Q., Zhang, C., Chen, H., et al., 2017. Size-resolved chemical composition, effective density, and optical properties of biomass burning particles. Atmos. Chem. Phys. 17, 7481-7493.

Zhang, R., Khalizov, A. F., Pagels, J., Zhang, D., Xue, H., and McMurry, P. H., 2008. Variability in morphology, hygroscopicity, and optical properties of soot aerosols during atmospheric processing. Proceedings of the National Academy of Sciences. 105, 10291.

Zhang, X., Lin, Y.-H., Surratt, J. D., and Weber, R. J., 2013. Sources, Composition and Absorption Ångström Exponent of Light-absorbing Organic Components in Aerosol Extracts from the Los Angeles Basin. Environmental Science & Technology. 47, 3685-3693.

Zuidema, P., Redemann, J., Haywood, J., Wood, R., Piketh, S., Hipondoka, M., et al., 2016. Smoke and Clouds above the Southeast Atlantic: Upcoming Field Campaigns Probe Absorbing Aerosol's Impact on Climate. Bulletin of the American Meteorological Society. 97, 1131-1135.

Figures and Captions
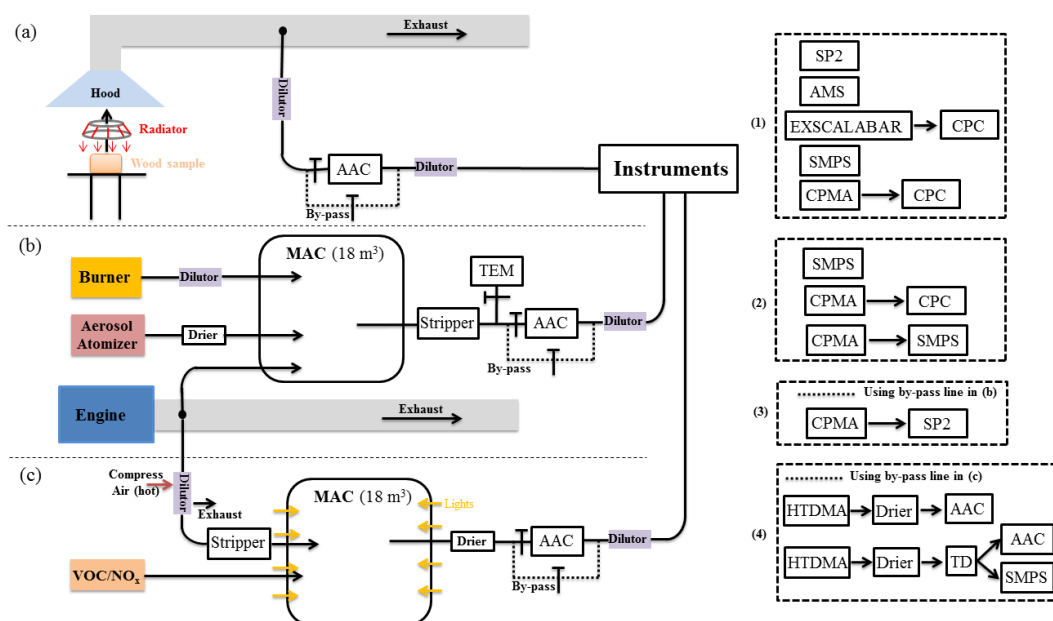
Fig. 1. Schematic diagram of the experimental configuration for: (a) Wood combustion; (b)

SP2 incandesces signal calibration and BC morphology investigation; (c) Brown carbon

formation and restructuring of BC. The combinations of instruments described in (1), (2), (3)

and (4) represent different measurement configurations used to enable characterisation of

specific aerosol physiochemical parameters, as described in the main text.
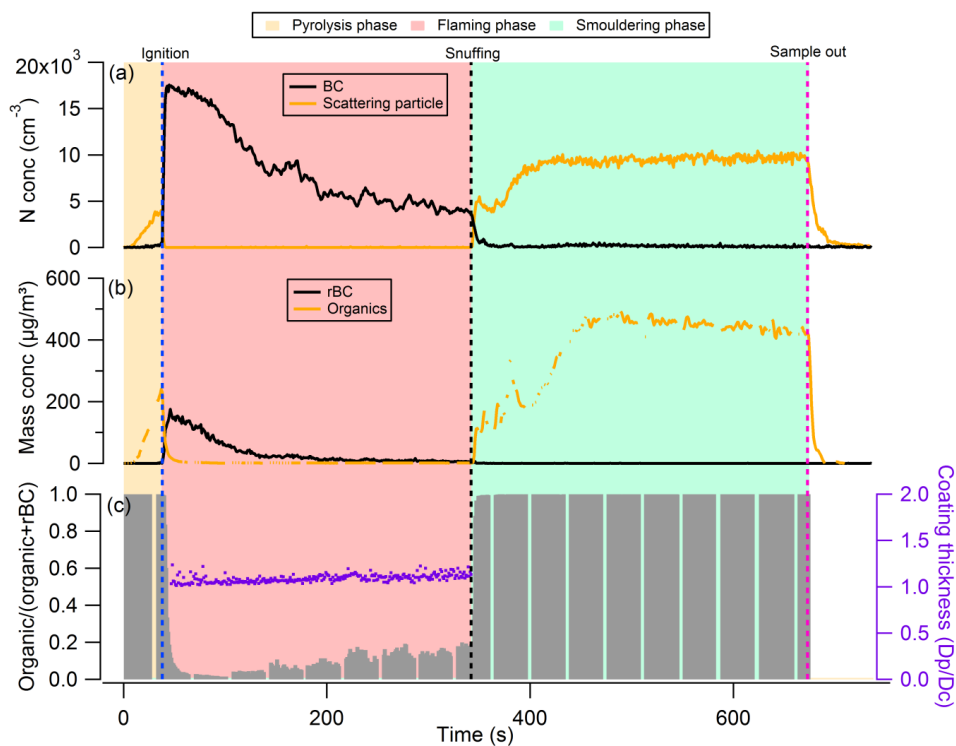
Fig. 2. Example of the phase transitions between different burn phases of dry Giant Redwood:

(a) number concentration of black carbon and the scattering particles detected from SP2; (b)

mass concentration of rBC and organics measured by SP2 and AMS, respectively; and (c)

mass ratio of organic aerosol to total aerosol.
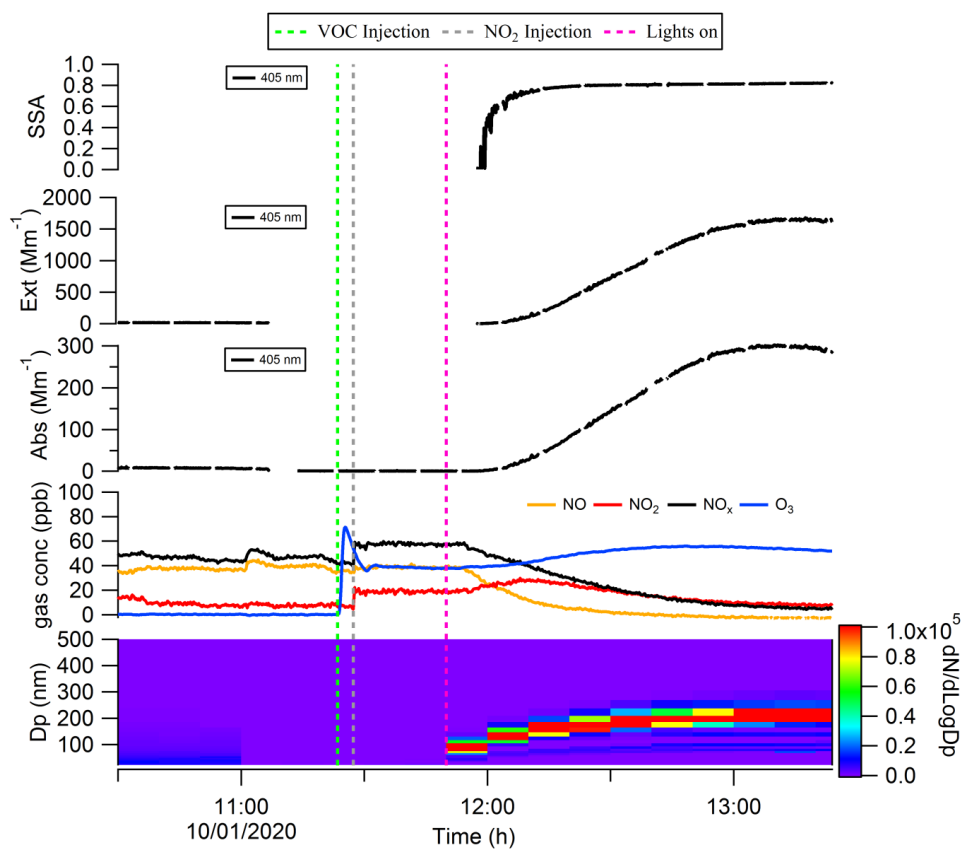
Fig. 3. Formation and evolution of the brown carbon with the precursor of cresol and NO_x in the chamber.
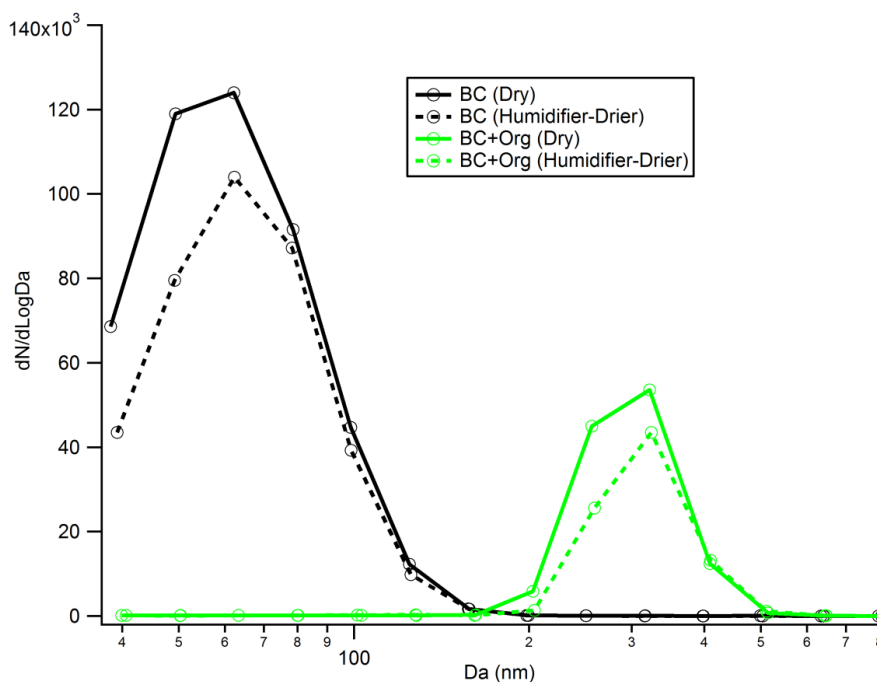
Fig. 4. Number size distribution of the bare BC (black line) and organic coated BC particles (green line) before and after they experience 'humidity cycling' (i.e. exposed to 90% RH around 10 s and then dehydrated to 10% RH) process. Da is the aerodynamic diameter.
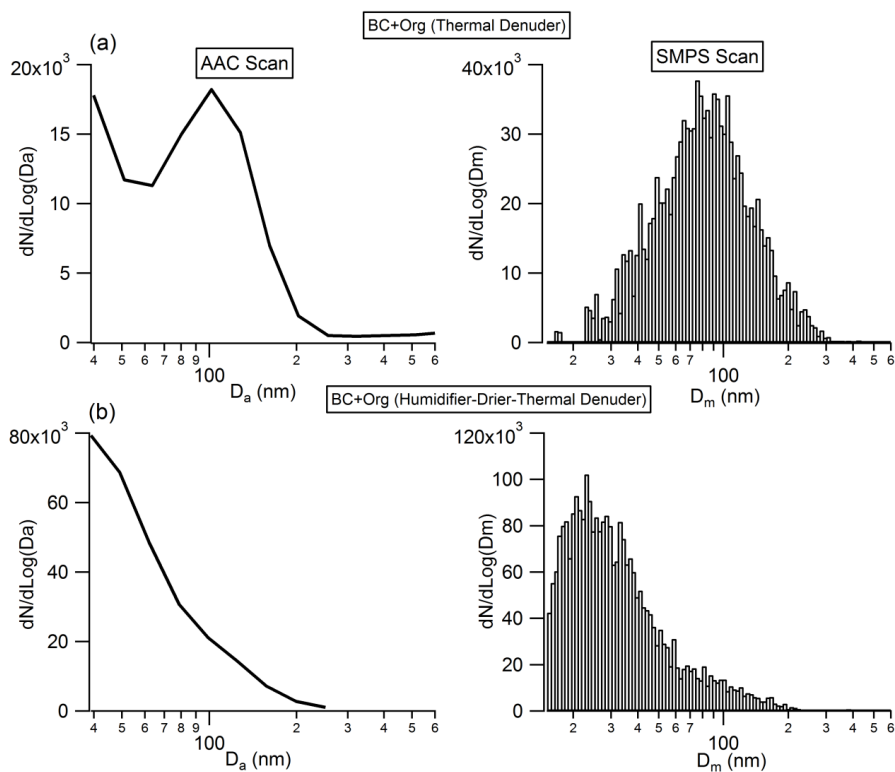
Fig. 5. Number size distribution of the: (a) organic coated BC after passing through the thermal denuder to remove coatings; and (b) organic coated BC after experiencing the 'humidity cycling' process and then passing through the thermal denuder to remove coatings.
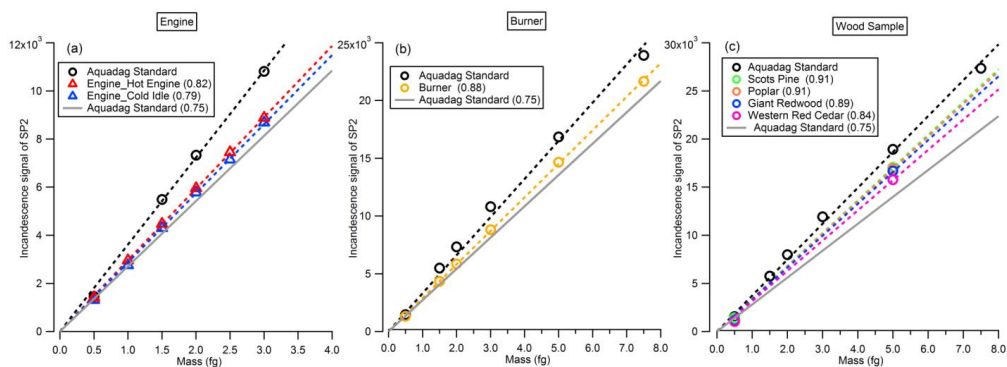
Fig. 6. The incandescence signal of the SP2 as a function of the rBC mass, BC particles were selected by the CPMA from: (a) engine emission; (b) burner emission; or (c) wood combustion emission.
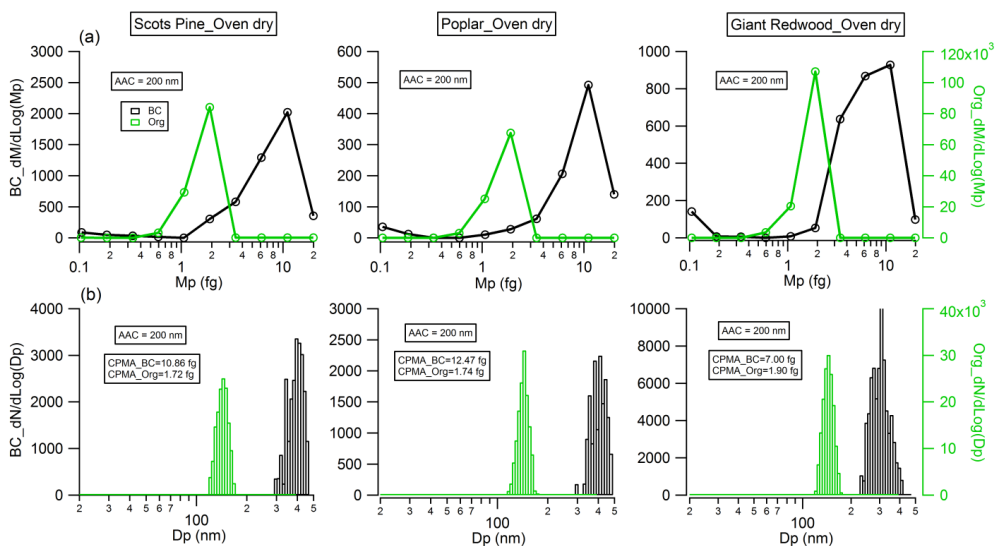
Fig. 7. Physical properties of mono-disperse (D_a=200 nm) black carbon (flaming phase) and organic particles (smouldering phase) emitted from wood combustion: (a) mass distribution measured by CPMA; (b) particle number distribution measured by the SMPS after the CPMA selected particles at the mass peak of the monodisperse (D_a=200 nm) particle mass distribution presented in (a).
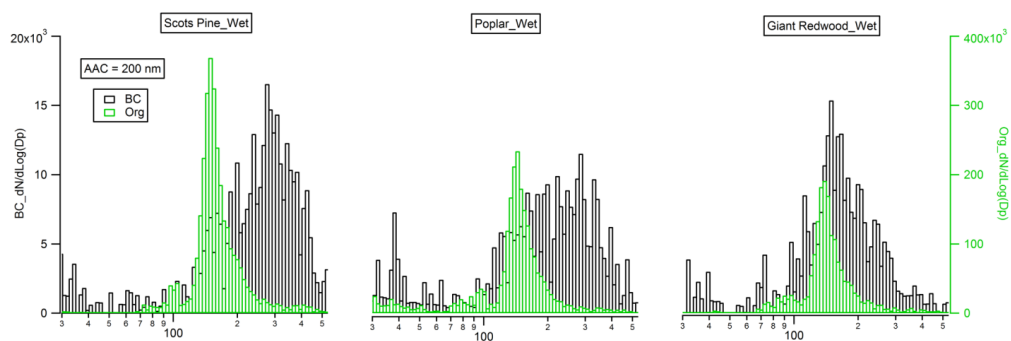
Fig. 8. Mobility size distribution of mono-disperse (D_a=200 nm) black carbon (flaming phase) and organic particles (smouldering phase) emitted from the combustion of the wet wood samples.
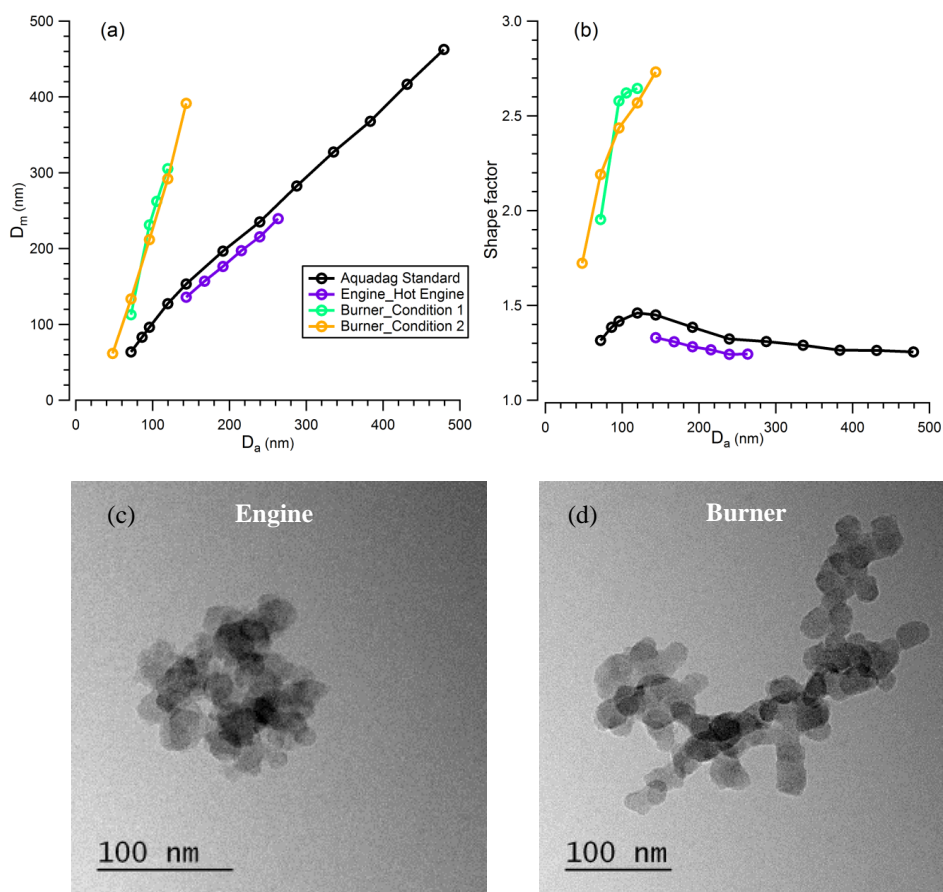
Fig. 9. Relationship of: (a) mobility size with aerodynamic size, and (b) shape factor with aerodynamic size, of BC particles from Aquadag standard atomization, diesel engine and flame burner emission; TEM images of BC particles emitted from: (c) diesel engine (hot engine condition) and (d) flame burner (condition 1).
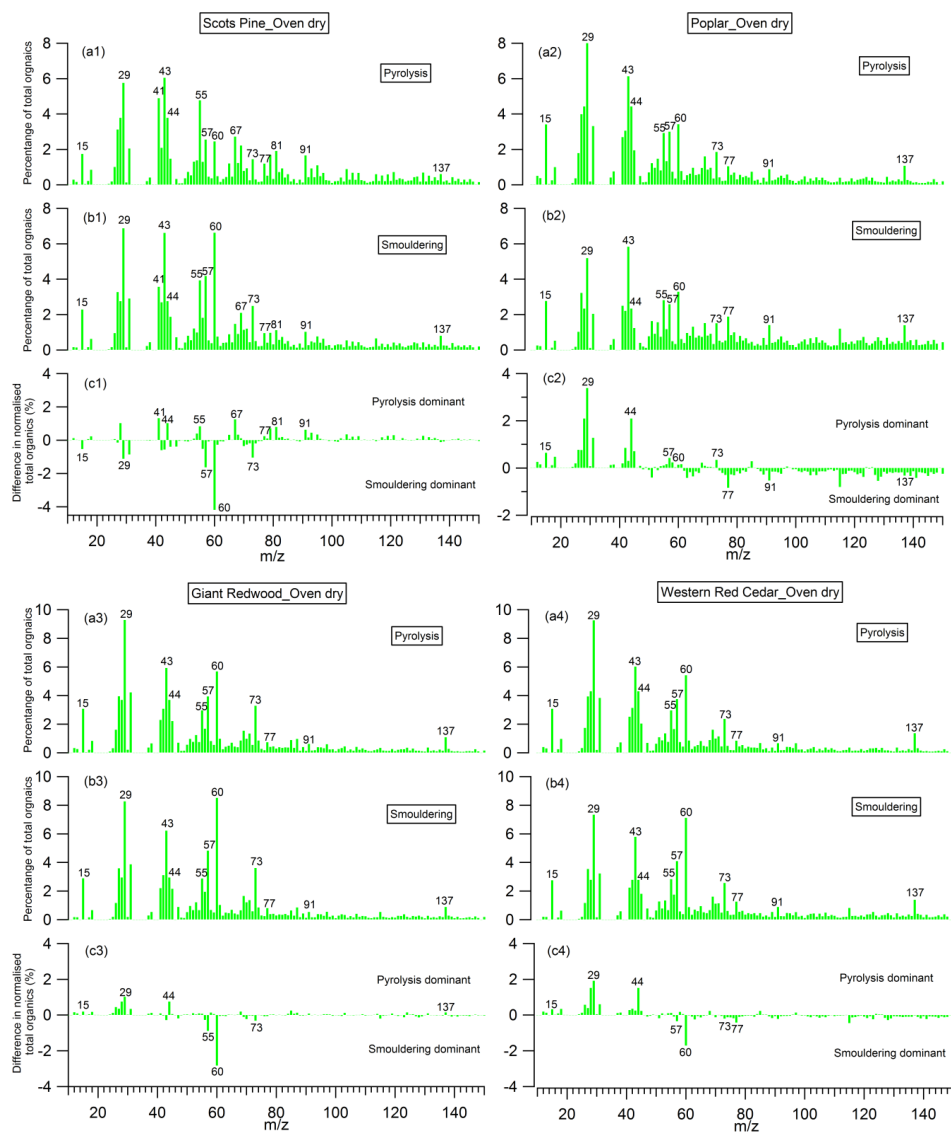
Fig. 10. Mass spectra of organic aerosols (OA) presented as a percentage of total OA produced during: (a) pyrolysis phase; (b) smouldering phase; and (c) the difference between them; for the dry wood samples.
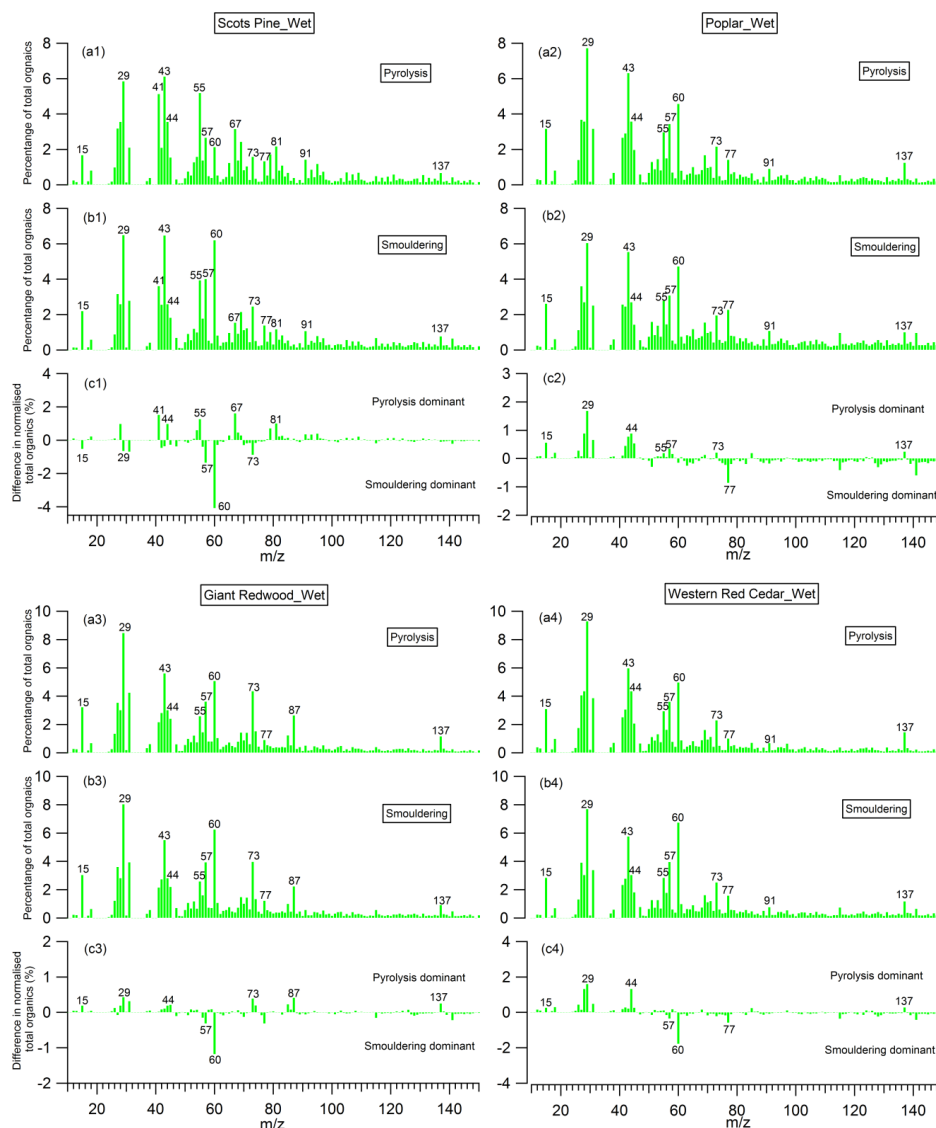
Fig. 11. Mass spectra of organic aerosols (OA) presented as a percentage of total OA produced during: (a) pyrolysis phase; (b) smouldering phase; and (c) the difference between them; for the wet wood samples.

Table and Caption

Table 1. Effective density and dynamic shape factor of organic and black carbon aerosols from wood combustion.

	Flaming phase_BC		Smouldering phase_Org	
	χ		ρ_m	
	Oven dry	**Wet**	**Oven dry**	**Wet**
Scots Pine	2.17[a]	1.85[a]	1.22[b]	1.44[b]
Poplar	2.10[a]	1.67[a]	1.23[b]	1.52[b]
Giant Redwood	1.80[a]	1.20[a]	1.32[b]	1.60[b]

[a] The BC density of 1.8 g/cm^3 was applied.
[b] Assuming organic aerosol is spherical with the shape factor of 1.00.